catalysts

MDPI

Article

Solketal Production Using Eco-Friendly Reduced Graphene Oxide as the Catalyst

Vinicius Rossa [1,2], Sancler da Costa Vasconcelos [1], Gisel Chenard Díaz [2], Josué de Almeida Resende [2], João Pedro Reys Mattos [1], Vinicius Gomes da Costa Madriaga [1], Fernanda Franco Massante [3], Yordanka Reyes Cruz [2], Juan Lucas Nachez [4], Yutao Xing [5], Eduardo Ariel Ponzio [3] and Thiago de Melo Lima [1,*]

1 Group of Catalysis and Biomass Valorization, Institute of Chemistry, Universidade Federal Fluminense, Niterói 24020-141, RJ, Brazil; drviniciusrossa@gmail.com (V.R.); sanclervasconcelos@id.uff.br (S.d.C.V.); jpreysmattos@id.uff.br (J.P.R.M.); vinicius_madriaga@id.uff.br (V.G.d.C.M.)
2 GreenTec Laboratory, School of Chemistry, Universidade Federal do Rio de Janeiro-EQ-UFRJ, Rio de Janeiro 21941-909, RJ, Brazil; gisemarina@yahoo.es (G.C.D.); yordanka@eq.ufrj.br (Y.R.C.)
3 Grupo de Eletroquímica e Eletroanalítica, Laboratório de Materiais, Institute of Chemistry, Universidade Federal Fluminense, Niterói 24020-141, RJ, Brazil; fernandafm@id.uff.br (F.F.M.); eduardoariel@id.uff.br (E.A.P.)
4 INFES, Institute of Physics, Universidade Federal Fluminense-IQ-UFF, Niterói 28470-000, RJ, Brazil; jlnachez@id.uff.br
5 Laboratório de Microscopia Eletrônica de Alta Resolução, Institute of Physics, Universidade Federal Fluminense-IQ-UFF, Niterói 24210-346, RJ, Brazil; xy@id.uff.br
* Correspondence: tmlima@id.uff.br

Abstract: In this study, two materials based on reduced graphene oxide (rGO_H or rGO_E) were synthesized through the Hummers methodology and a more sustainable electrochemical method. These materials were extensively characterized and tested as catalysts in solketal production. Both rGO_H and rGO_E demonstrated significant catalytic activity, achieving 66.18% and 63.97% conversion rates, respectively. The catalytic activity of the synthesized materials was 30 times more efficient than the homogeneous catalyst *p*-Toluenesulfonic acid. Pseudo-homogeneous and heterogeneous kinetic models were employed to gain further insights into the glycerol ketalization reaction with acetone. The pseudo-homogeneous model suggested that the direct rate constant was lower than the reverse rate constant. In this sense, a reversible bimolecular reaction was proposed. The heterogeneous kinetic models revealed that in the Langmuir-Hinshelwood-Hougen-Watson mechanism, the controlling step of the reaction was the glycerol-acetone surface reaction on the catalyst. In contrast, in the Eley-Rideal mechanism, the reaction was controlled by the adsorbed glycerol on the reaction surface reacting with the available acetone in the bulk fluid. In the reusability tests, the rGO_E catalyst demonstrated superior performance over five consecutive cycles, maintaining the highest activity without needing post-reaction washing or treatment.

Keywords: glycerol; solketal; reduced graphene oxide; kinetic evaluation

check for updates

Citation: Rossa, V.; Vasconcelos, S.d.C.; Díaz, G.C.; Resende, J.d.A.; Mattos, J.P.R.; Madriaga, V.G.d.C.; Massante, F.F.; Cruz, Y.R.; Nachez, J.L.; Xing, Y.; et al. Solketal Production Using Eco-Friendly Reduced Graphene Oxide as the Catalyst. *Catalysts* **2023**, *13*, 1427. https://doi.org/10.3390/catal13111427

Academic Editors: Domenico Licursi and Juan Hernández Adrover

Received: 16 October 2023
Revised: 5 November 2023
Accepted: 7 November 2023
Published: 10 November 2023

1. Introduction

Biofuel research has attracted attention recently as an energy transition is occurring, as seen in global discussions. Biodiesel is a notable example in this context, as its production is commonly achieved through the transesterification of triglycerides. Furthermore, biodiesel is already established in the fuel market. However, as its production increases, other issues related to the process arise, particularly concerning glycerol production [1,2]. The transesterification reaction generates glycerol as a byproduct, and it is estimated that for every liter of biodiesel produced, 100 mL of glycerol is generated. However, this compound has industrial demand, which can result in various problems related to its accumulation and transportation [3].

Glycerol chemistry has emerged as a distinct branch to enhance the value of glycerol through chemical transformations involving various reactions. These reactions include carbonation, dehydration, hydrogenolysis, and oxidation [4,5]. All of these resulting products find distinct applications across multiple industry sectors, serving as solvents, additives, plasticizers, disinfectants, and more [6]. However, the ketalization reaction stands out as it produces one of the most versatile compounds in the industry: solketal. This compound finds numerous applications in green solvents and fuel additives and is also relevant to the pharmaceutical and food industries. The production of solketal involves the ketalization of glycerol (as depicted in Scheme 1), resulting in the byproduct dioxan. In this sense, it is essential to note that an acid catalyst is necessary to facilitate this reaction [5,7].

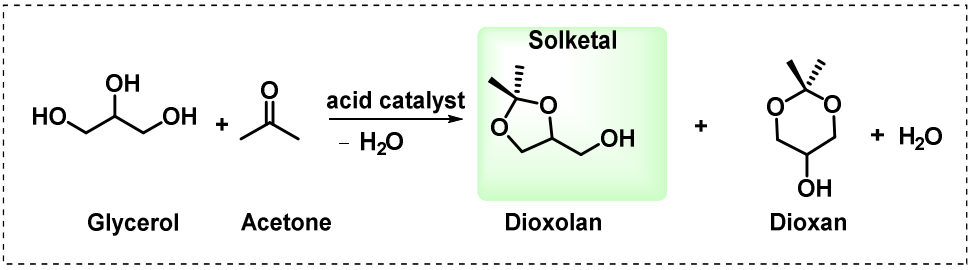

Scheme 1. Glycerol ketalization reaction with acetone producing solketal and dioxan.

As previously mentioned, selecting a catalyst is critical in successfully producing solketal. Moreover, from a green perspective, catalysis can expedite this process, reducing reaction times and temperatures in certain instances. Recently, heterogeneous catalysts have gained preference due to their favorable environmental and economic attributes. Their reusability and scalability are comparatively more straightforward, making them more practical than other types of catalysts. Additionally, these materials can be easily separated from the reaction medium, simplifying downstream processes and reducing waste generation [8,9].

Numerous heterogeneous catalysts have been proposed for glycerol ketalization, including zeolites [10,11], mesoporous silicas [11], and others. Some of these materials have achieved up to 98% conversion in certain instances, making them desirable due to their high surface area and acidity. Among these catalysts, carbon-based materials have been proposed for solketal production primarily because of their unique surface properties. For example, Rodrigues and coworkers [12] studied activated carbons as catalysts for solvent-free ketalization, achieving 52% conversion and 97% selectivity for solketal. However, despite the potential of carbon materials, only a few studies have explored these catalysts.

From this point of view, graphene and its derivatives exhibit significant potential for application as catalysts. This is attributed not only to their surface properties and thermochemical stability but also to the fact that their acidity can be adjusted through established procedures [13]. For example, graphene oxide (GO) already possesses intrinsic acidity due to phenolic and carboxylic groups on its surface. Additionally, reduced graphene oxide (rGO) is an exciting derivative since it exhibits acidity, primarily due to oxygenated functional groups at the layer edges and the presence of a graphitic aromatic structure [14]. However, the production of these materials is not environmentally friendly. As the Hummers method exemplifies, classical methods for obtaining graphene and its derivatives are frequently hazardous and result in significant waste generation. From a green chemistry perspective, adopting more sustainable approaches to minimize the environmental impact is imperative [15].

The Hummers method involves high concentrations of acidic media and manganese-based reagents [15]. However, as previously mentioned, it is imperative to discover more environmentally friendly methods for producing rGO to minimize waste generation. Electrochemical exfoliation involves the production of rGO_E through electrolysis, utilizing a graphite electrode as the anode. This process leads to the oxidation of graphite into

rGO, followed by its subsequent deposition [16]. In this study, both reduced graphene oxides obtained through distinct synthesis pathways were employed and compared in relation to solketal production. Additionally, their chemical and surface properties were investigated. In this context, this paper's contribution to the specialized literature is the electrochemical exfoliation of graphite for obtaining rGO_E without hazardous chemicals, using an eco-friendly pathway for the efficient production of solketal. In addition, this paper advances catalyst reuse, in which the material can maintain its activity even after three reuse reactions without washing or purification steps. In this sense, we demonstrate here that an eco-friendly rGO can be produced with high acidity and that it is a promising material to be used as a catalyst for other acid-catalyzed reactions.

2. Results

2.1. Crystalline and Spectroscopic Characterization of Carbon-Derived Materials

Figure 1 shows the diffractograms obtained for the GFT_H, rGO_H, GFT_E, and rGO_E materials. The X-ray diffractogram of GFT_H (graphite flakes), in Figure 1a, shows a peak at 2θ = 26.32° with high intensity, indicating high crystallinity in the material [17]. On the other hand, the diffractogram of rGO_H (reduced graphene oxide Hummers method), in Figure 1b, exhibits a significant reduction in this peak intensity compared to graphite, suggesting a considerable loss of crystallinity in the material, highlighting the efficiency of the graphite exfoliation process in forming rGO_H. The lower peak intensity at 2θ = 13.29° in rGO_H indicates low efficiency in the samples' oxidative processes, suggesting minimal material oxidation and direct formation of reduced graphene oxide [18].

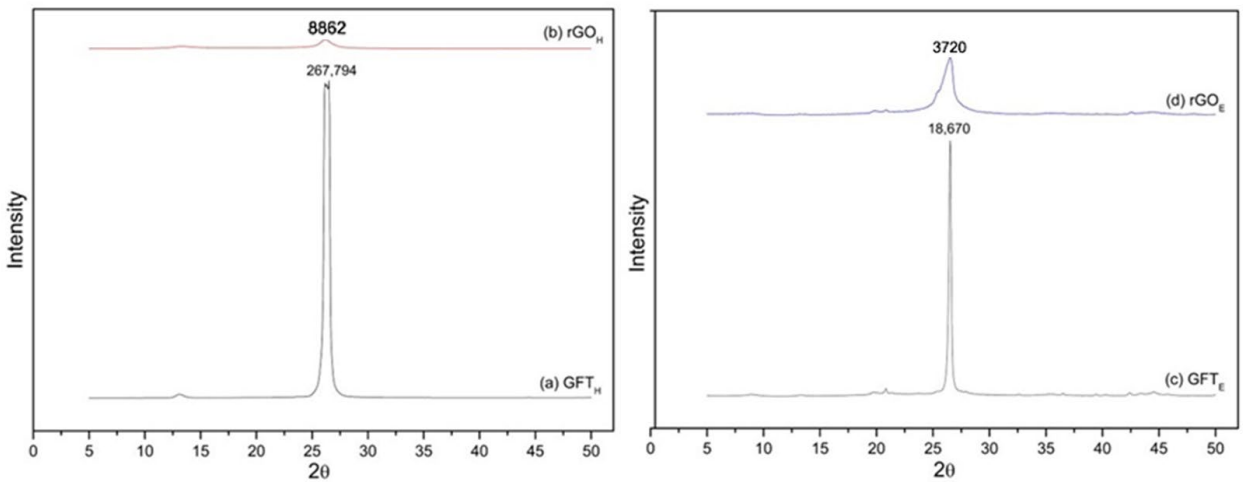

Figure 1. X-ray diffractograms of graphite flakes (**a**) GRF_H, (**b**) rGO_H, (**c**) GFT_E, and (**d**) rGO_E.

The graphite from the carpenter's pencil (GFT_E), in Figure 1c, exhibits a characteristic graphite peak diffracted at 2θ = 26.51° in the (001) plane with high intensity, indicating high crystallinity for this material. After the oxidative exfoliation process, in Figure 1d (rGO_E), the peak shifted slightly to 2θ = 26.29°, and there was a significant loss of crystallinity and structural disorganization when compared to its starting material (GFT_E), indicating the efficiency of the exfoliation process [19].

Through XRD analysis, important information was obtained, which enabled the determination of distances between layers using Bragg's Law, average crystallite sizes through Scherrer's Equation, and the number of stacked layers in the materials GFT_H, rGO_H, GFT_E, and rGO_E, as shown in Table S1 [20–24].

Table S1 shows a slight increase in the distance difference between the layers of the carbon-based materials, indicating the low degree of graphite oxidation. However, there was a high exfoliation of 44 layers in the GFT_H precursor material and 17 layers in the rGO_H, respectively. The exfoliation via the electrochemical method proved to be more efficient than the Hummers method, with 91 layers in the $GRFT_E$ precursor and 15 layers in rGO_E.

There was also a significant decrease in the crystallite size of the precursor materials GFT_H and GFT_E (15 and 31 nm, respectively) when compared with the size of the crystallites of the rGO_H and rGO_E (5 nm).

Next, Raman spectroscopy was utilized to enhance comprehension of the oxidation processes. Generally, in the Raman spectra of graphite and reduced graphene oxide, two characteristic bands can be observed: The D Band (defects in the structure), with A_{1g} symmetry, located between 1350 and 1360 cm^{-1} [25–27], attributed to oxygenated groups in the basal plane of the graphene derivatives' structure [26] during sp^3 hybridization of carbon in the layers [28]. The G Band is present in ordered graphene networks (E_{2g} symmetry), with high intensity located between 1580 and 1610 cm^{-1} [25–27], attributed to sp^2 hybridization [27]. Figure 2 presents the Raman spectra for the GFT_H, rGO_H, GFT_E, and rGO_E materials.

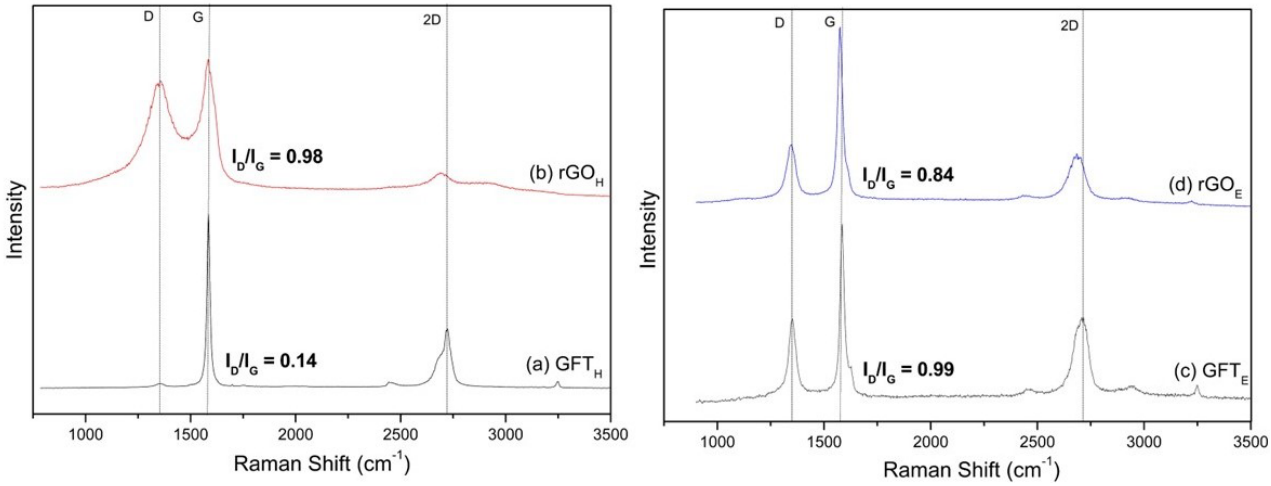

Figure 2. Raman spectra of graphite flakes (**a**) GRF_H, (**b**) rGO_H, (**c**) GFT_E, and (**d**) rGO_E.

Figure 2a presents the D band of GFT_H, corresponding to the vibrational mode of sp^3 hybridized carbon atoms with a minimum intensity at 1341 cm^{-1}, which occurs due to the high organization of carbon atoms with sp^2 hybridization [27,29,30]. Conversely, the D band of rGO_H, in Figure 2b, shows an increase in intensity at 1347 cm^{-1}, attributed to structural disorganization after the exfoliation–oxidation process. However, this increase in the intensity of the D band indicates the rupture of C=C bonds during the oxidation of GFT_H to rGO_H and an increase in sp^3 hybridized carbon atoms [27,29,30]. This is due to imperfections created via the insertion of oxygenated groups in the basal plane of the carbon layers, leading to partial structural disorder [27,29,30]. The G band decreased with the oxidation of GFT_H, seen in Figure 2a, located at 1583 cm^{-1}, while for rGO_H, seen in Figure 2b, it was observed at 1580 cm^{-1}. The rGO_H structure resulted in a higher I_D/I_G intensity ratio due to defects in GFT_H (I_D/I_G = 0.14), and after the exfoliation–oxidation process due to rGO_H (I_D/I_G = 0.98) [27,29,30]. The Raman spectrum of GFT_E presented a D band of graphite with low intensity at 1354 cm^{-1} (sp^3 hybridized carbon atoms) due to the high organization of carbon atoms with sp^2 hybridization.

On the other hand, this band in rGO_E displayed an increase in intensity due to structural disorganization after the exfoliation of GFT_E via the electrochemical method. This increase is attributed to imperfections created via the insertion of oxygenated groups in the basal plane of the carbon layers, leading to partial structural disorder. The G band, corresponding to the vibrational mode of sp^2 hybridized carbon atoms, decreased in the GFT_E material after its exfoliation to produce rGO_E [30]. The analyses of the I_D/I_G results for the rGO_H and rGO_E materials and a comparison of them with their precursor materials showed a structural rearrangement in the formation of reduced graphene oxides [30], corroborating the XRD results.

The 2D or 'G' band, ranging between 2600 cm^{-1} and 2800 cm^{-1}, is a broad hump associated with the interplanar stacking order, the number of layers, and even the in-plane order of the crystallite size for graphene materials. According to Malard and coworkers [31], the presence of the 2D (G′) band is attributed to second-order two-phonon processes of the sp^2 carbon structure. A broader 2D band implies an increased number of graphene layers.

The broader 2D region for rGO_H shows a lower intensity when compared with rGO_E. This indicates that the exfoliation of rGO_H results in more pronounced overlapping GO layers when compared with rGO_E. On the other hand, the higher intensity of the G peak compared to the D peak for rGO_E when compared with rGO_H suggests that there is more graphene oxide than graphene sheets or graphite.

To determine the oxygenated groups introduced to the graphites after the exfoliation–oxidation process, infrared spectroscopy was utilized. Figure S2 presents the infrared spectra obtained for the GFT_H, rGO_H, GFT_E, and rGO_E materials. The spectrum of GFT_H graphite, seen in Figure S2a, exhibits bands related to the vibrations of C sp^2 bonds in the graphene layers that constitute the graphite. A low-intensity band at 3488 cm^{-1} is attributed to –OH group bonds, and a band at 1409 cm^{-1} indicates the presence of –COOH bonds from the carboxyl group, suggesting that GFT_H has a low degree of oxidation. In the spectrum of rGO_H, in Figure S1b, a band appeared at 3338 cm^{-1}, corresponding to –OH group bonds. This indicates the insertion of –OH groups into the GFT_H structure during graphite's exfoliation/oxidation process. Additionally, in Figure S2b, the insertion of oxygenated groups into the graphite structure is observed, including carbonyls (1578 cm^{-1}); carboxyls (1409 cm^{-1}); alcohols and phenols (1388 cm^{-1}, 1247 cm^{-1}); and epoxide groups (1076 cm^{-1}), as reported in the literature [20,25,28,32–37].

The spectrum of GFT_E graphite, in Figure S2c, exhibits bands related to the vibrations of C sp^2 bonds in the graphene layers in the graphite structure. A low-intensity band at 3369 cm^{-1} is attributed to –OH group bonds, and a band at 1158 cm^{-1} indicates the presence of C–O bonds of alcohols and phenols, suggesting that GFT_E presents some degree of oxidation. In the spectrum of rGO_E, in Figure S2d, an intense peak appears at 3360 cm^{-1}, corresponding to –OH group bonds, indicating the insertion of –OH groups into the GFT_E structure during the exfoliation process of graphite. Figure S2d shows that the oxygenated groups inserted into the graphite structure after the exfoliation/oxidation process via the electrochemical method include carbonyls (1538 cm^{-1}); carboxyls (1444 cm^{-1}); alcohols and phenols (1365 cm^{-1}, 1234 cm^{-1}, 1204 cm^{-1}, 1158 cm^{-1}, and 1121 cm^{-1}); and epoxide groups (1051 cm^{-1}), as reported in the literature [20,25,27,28,32–38]. Also, Table S2 shows the assignments of the prominent bands in the infrared spectra for the GFT_H, rGO_H, GFT_E, and rGO_E materials.

2.2. Thermal and Textural Characterization of Carbon-Derived Materials

Thermogravimetric analyses (TGAs) were employed to assist in the study of the insertion of oxygenated groups into the structures of commercial graphites to form rGOs. Figure 3 presents the weight loss curves of the materials for the GFTH, rGOH, GFTE, and rGOE materials.

The GFT_H presented two weight loss events. The first, between 25 and 470 °C, was attributed to the loss of water molecules adsorbed on the surface and trapped between the layers of the material, resulting in a mass loss of 0.60%. The second event was assigned to decompose the more stable graphite layers (formed via sp^2 hybridized carbon), leading to a mass loss of 22.95%. GFT_H was the most stable among the materials, with a total mass loss of 23.55% [21,28,33,34,38,39]. Its reduced graphene-oxide-derived material also presented six weight loss events, with the first at 107 °C, which was attributed to the loss of surface-adsorbed water, resulting in a mass loss of 3.88%. At 228 °C, the second event was assigned to decomposing less stable functional groups in the rGO structure, with a weight loss of 12.07%. The third, at 367 °C, was attributed to the decomposition of more stable functional groups in the rGO structure, with a weight loss of 7.27%. The fourth, at 450 °C, was also assigned to decomposing more stable functional groups in the rGO

structure, resulting in a weight loss of 6.65%. At 507 °C, the fifth event was attributed to the decomposition of less stable rGO layers (formed via sp^3 hybridized carbon); the most prominent weight loss event was 66%. Finally, at 663 °C, the sixth event was attributed to the decomposition of the more stable rGO layers (formed via sp^2 hybridized carbon), resulting in a weight loss of 2.71%. At the end of the analysis, only 0.69% of the original mass remained, indicating almost complete degradation of the rGO_H. The carpenter pencil presented four events, as seen in Figure 3c. The first, at 83 °C, was attributed to the loss of water molecules adsorbed on the surface of the graphite, with a weight loss of 0.28%. The second, at 150 °C, was assigned to the loss of water trapped between the layers of the graphite, resulting in a weight loss of 3.20%. The third, at 292 °C, was attributed to the pyrolysis of less stable and partially oxidized graphite layers, releasing CO, CO_2, and H_2O, with a mass loss of 6.80%. This result agrees with the infrared spectrum of GFT_E, seen in Figure 3c. The last thermal event, at 640 °C, was assigned to decomposing the more stable graphite layers (formed via sp^2 hybridized carbon), resulting in the most significant weight loss of 39.12%. However, the total mass loss of the GFT_E was 49.22%, making it the most stable compared to the other studied materials. In addition, the rGO_E material presented six events, seen in Figure 3d. The first, at 195 °C, was attributed to the loss of water molecules adsorbed on the surface of rGO_E, with a weight loss of 3.86%. At 258 °C, the second was assigned to decomposing less stable oxygenated functional groups in the rGO structure, with a weight loss of 1.67%. The third, at 308 °C, was attributed to the decomposition of more stable oxygenated functional groups in the rGO structure, resulting in a weight loss of 1.93%. The fourth, at 593 °C, was assigned to decomposing more stable functional groups in the rGO structure, leading to a weight loss of 12.65%. The fifth, at 615 °C, was attributed to the continuation of the decomposition of more stable functional groups in the rGO_E structure and sp^3 carbons, with a mass loss of 21.30%. The sixth and final event, at 703 °C, was assigned to the decomposition of rGO layers (sp^2 carbons), resulting in the most extensive mass loss of 34.68%. rGO_E showed a total weight loss of 76.09% of its initial mass [21,28,33,34,38,39].

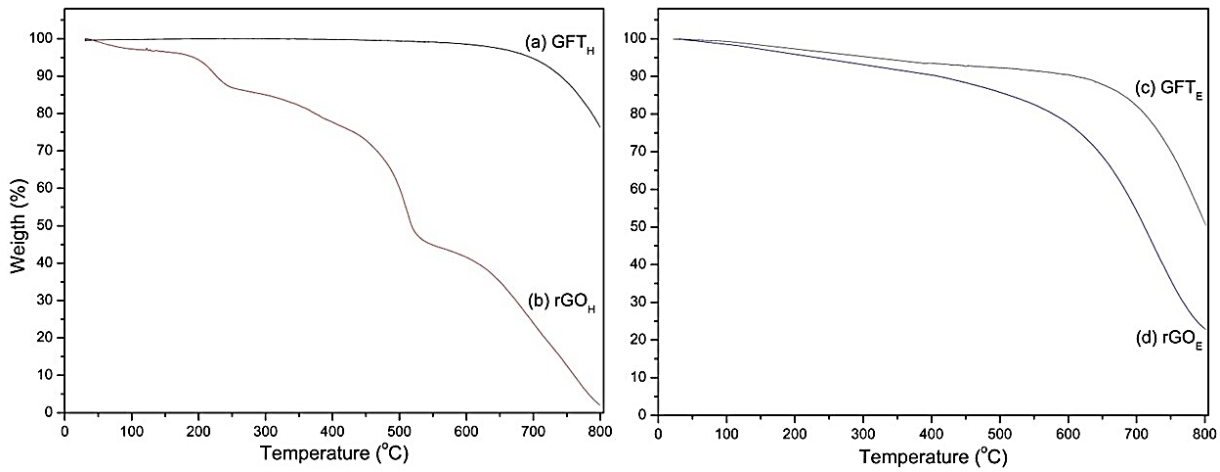

Figure 3. Thermogravimetric analysis of graphite flakes (**a**) GRF_H, (**b**) rGO_H, (**c**) GFT_E, and (**d**) rGO_E.

To test rGO_H and rGO_E as catalysts for the glycerol ketalization reaction [40], these materials and their precursors were also characterized via textural and porosity analysis using the B.E.T., t-plot, and B.J.H. methods, as well as via morphological analysis through scanning electron microscopy (SEM). Table 1 presents the results from the textural characterization for the GFTH, rGOH, GFTE, and rGOE materials via N_2 sorption analysis.

Table 1. Textural characterization of the GFT_H, rGO_H, GFT_E, and rGO_E materials.

	Materials			
	GRF_H	**rGO_H**	**GRF_E**	**rGO_E**
Specific superficial area (m^2 g^{-1})	5.1	31.0	4.3	21.3
Micropore volume (cm^3 g^{-1}) [1]	-	0.0008	-	0.0005
Mesopore volume (cm^3 g^{-1}) [2]	0.062	0.053	0.050	0.047
Average size pore (nm)	10.9	10.3	10.9	10.2

[1] Calculated using t-plot method; [2] calculated using B.J.H. method.

2.3. Morphological Characterization of Carbon-Derived Materials

The specific surface areas of GFT_H and GFT_E were 5.1 and 4.3 m^2 g^{-1}, respectively, which are very close to the values found in the literature, ≈4 m^2 g^{-1} [41,42]. The rGO_H showed a specific surface area of 31.0 m^2 g^{-1}; in rGO_E, this area was 21.3 m^2 g^{-1}. The electrochemical process typically produces rGO with a lower specific surface area than the exfoliation–oxidation carried out via the traditional Hummers method [43,44]. Both rGO_H and rGO_E exhibited larger specific surface areas than their precursor materials, suggesting that the exfoliation process was effective. This exfoliation is better verified with the aid of morphological analyses conducted using scanning electron microscopy, as shown in Figure 4, which displays the micrographs of the GFT_H, rGO_H, GFT_E, and rGO_E materials.

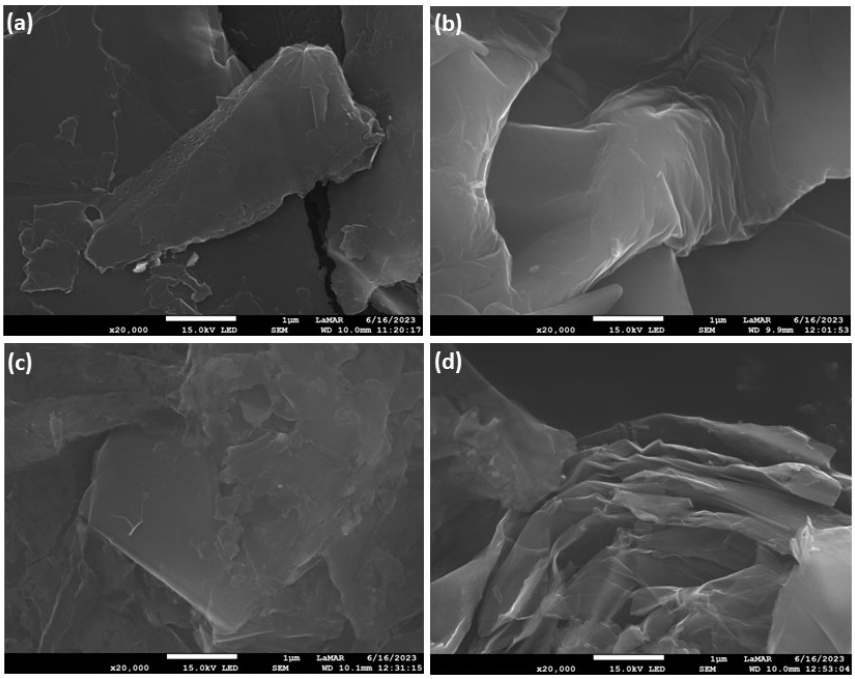

Figure 4. SEM images of graphite flakes (**a**) GRF_H, (**b**) rGO_H, (**c**) GFT_E, and (**d**) rGO_E.

Figure 4a,c display the SEM images of GFT_H and GFT_E, respectively, illustrating the morphology of graphite flake and carpenter's pencil graphite. These images reveal a morphology consisting of densely packed graphene sheets. Upon oxidation and exfoliation processes to form rGO_H and rGO_E, as shown in Figure 4b,d, there was an observable increase in spacing and disorganization between these sheets. In a morphological analysis conducted by Basso and coworkers [20], they observed similar morphology changes during the transition from graphite to rGO due to oxidation [20].

Energy Dispersive X-ray Spectroscopy (EDS) analyses were conducted during SEM analysis to investigate the materials' surface chemical compositions. The results of the surface chemical compositions of the materials are presented in Table 2.

Table 2. EDS results of surface chemical analysis of the GFT_H, rGO_H, GFT_E, and rGO_E materials.

	Elements (wt.%)				
Materials	**C**	**O**	**S**	**Si**	**Al**
GRF_H	98.0	2.0	-	-	-
rGO_H	79.6	19.6	0.8	-	-
GRF_E	73.5	21.0	-	4.8	0.7
rGO_E	68.3	24.9	0.5	4.8	1.5

rGO_H exhibited an oxygen content of 19.6%, whereas its precursor material showed only 2%, thus indicating a low oxidation level of commercial graphite. In contrast, the commercial GRF_E already had a high oxidation level, with 21.0% oxygen on its surface. After its exfoliation/oxidation, the oxygen content increased to approximately 5% in rGO_E, representing 24.9%. Both rGO_E and GFT_E exhibited impurities like Si and Al. The rGO_H material and rGO_E showed 0.8% and 0.5% sulfur content, respectively, attributed to the sulfuric acid used in both rGO production processes.

Considering these characteristics, acidity tests were also conducted on rGO_H and rGOE. However, due to their low thermal stability, acidity was determined through acid–base titration, as presented in Table S3. These values indicate that the exfoliation/oxidation process used to obtain rGO_H and rGO_E makes these materials significantly acidic for application as catalysts in the glycerol ketalization reaction with acetone for solketal production.

2.4. Catalytic Activity and Kinetic Studies of Glycerol Ketalization

Table 3 presents the results obtained from preliminary catalytic tests, including control (blank/no catalyst), the homogeneous *p*-Toluenesulfonic acid (PTSA) catalyst, and the heterogeneous rGO_H and rGO_E catalysts, in terms of glycerol conversion (X_A).

Table 3. Results of preliminary catalytic tests for glycerol conversion (X_A%), solketal selectivity (SS_5), dioxan selectivity (SD_6%), solketal yield (YS_5%), and dioxan yield (YD_6%).

Reaction	X_A (%)	SS_5 (%)	SD_6 (%)	YS_5 (%)	YD_6 (%)	TOF (h^{-1})
Control	0.20 ± 0.02	80.39 ± 0.02	19.61 ± 0.02	0.16 ± 0.02	0.04 ± 0.02	-
PTSA	35.45 ± 0.64	97.71 ± 0.64	2.49 ± 0.64	64.32 ± 0.64	1.64 ± 0.64	1.80 ± 0.37
rGO_H	66.18 ± 0.45	98.38 ± 0.45	1.62 ± 0.45	51.00 ± 0.45	1.55 ± 0.45	52.36 ± 0.32
rGO_E	63.97 ± 0.86	80.73 ± 0.86	19.27 ± 0.86	51.64 ± 0.86	12.33 ± 0.86	57.44 ± 0.43

(Molar ratio of glycerol/acetone = 1:4; 5% catalyst based on the mass of glycerol; 60 °C; 500 rpm; 120 min with autogenous pressure; conducted in a 100 mL Parr reactor).

The influence of an acidic catalyst on the glycerol ketalization reaction with acetone is evident from the negligible glycerol conversion (X_A = 0.20%) in the control reaction. The homogeneous PTSA catalyst exhibited low activity for solketal conversion (35.45%) but high selectivity towards solketal (97.71%). However, the heterogeneous catalysts showed increased activity, with 66.18% and 63.97% conversion rates for rGO_H and rGO_E, respectively. Nonetheless, the rGO_E catalyst synthesized using the electrochemical method showed lower selectivity towards solketal (80.73%) than the other catalysts, where the selectivity for rGO_H and PTSA was 98.38% and 97.71%, respectively. However, it is essential to note that PTSA is a homogeneous catalyst that causes equipment corrosion and waste generation. In addition, the conventional graphene-derived material rGO_H is prepared via a non-sustainable procedure and produces much waste. The electrochemically produced graphene-derived material rGOE, despite presenting lower solketal selectivity, must be highlighted for its greener production.

The TOF values for PTSA, rGO_H, and rGO_E are presented in Table 3. The number of acid sites for the heterogeneous catalysts was obtained through the acidity determination via the acid–base titration technique (Table S3). The highest TOF value was 57.44 h^{-1}, achieved with the rGO_E catalyst after 2 h of reaction. The lowest TOF value was 1.80 h^{-1},

obtained with the PTSA catalyst. No significant difference was observed when comparing the TOF value for the heterogeneous catalysts, highlighting the potential application of rGO_E as a more sustainable catalyst.

Figure 5 presents the results obtained for glycerol conversion tests (X_A%) over time using the homogeneous PTSA catalyst and the heterogeneous rGO_H and rGO_E catalysts.

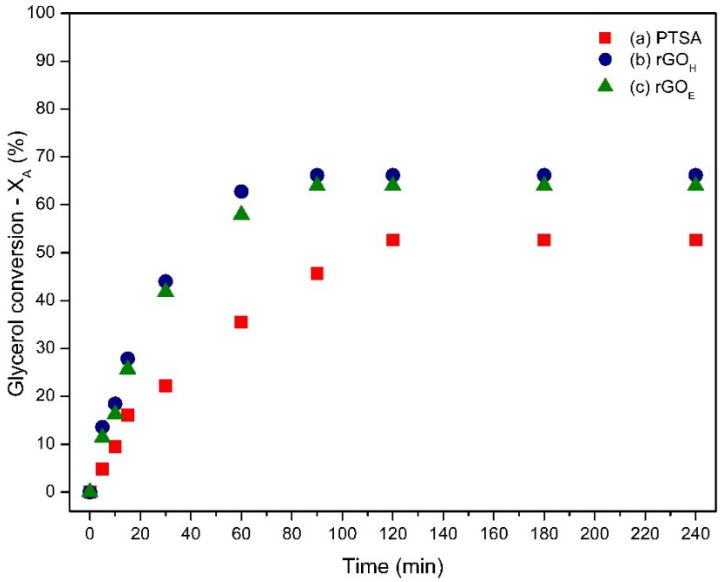

Figure 5. Results of glycerol conversion tests (X_A%) over time for the homogeneous catalyst PTSA and the heterogeneous catalysts rGO_H and rGO_E. (Glycerol/acetone molar ratio = 1:4; 5% catalyst relative to the mass of glycerol; 60 °C; 500 rpm with autogenous pressure; conducted in a 100 mL Parr reactor).

It can be observed that the rGO_H catalyst exhibited higher initial conversion values, converting approximately 19% of the glycerol in the first 10 min of the reaction. For comparison, rGO_E converted about 16% of the available glycerol simultaneously. Meanwhile, the homogeneous catalyst PTSA transformed 9% during the initial 10 min of the reaction. After 90 min of reaction, the glycerol conversion stabilized for the heterogeneous catalysts. This suggests that the reaction reached a steady state, with 66% and 64% conversion for rGO_H and rGO_E, respectively. The homogeneous catalyst PTSA was constant after 120 min of reaction.

Two approaches were considered to estimate kinetic parameters (k_1 and k_2) for the glycerol ketalization reaction in the presence of acidic catalysts: the pseudo-homogeneous and heterogeneous kinetic models.

Using the Python programming language and the data from Figure 5, through GOOGLE COLAB (https://colab.research.google.com/?utm_source=scs-index&hl=en, accessed on 5 November 2023), it was possible to estimate the values for the rate constants k_1 and k_2 for three different catalytic systems (PTSA, rGO_H, and rGO_E), and the estimated values are shown in Table 4.

Table 4. Estimated values for the rate constants k_1 and k_2 for three different catalytic systems (PTSA, rGO_H, and rGO_E). Conditions: 500 rpm; molar ratio 1:4 (G:A); 5% catalyst relative to the mass of glycerol; 60 °C; 240 min.

Catalysts	k_1	k_2	K	X_A	X_{Aeq}	Q	R^2
PTSA	0.0015	0.0077	0.1953	0.53	0.55	0.0024	0.9929
rGO_H	0.0037	0.0089	0.4184	0.66	0.67	0.0019	0.9966
rGO_E	0.0033	0.0092	0.3621	0.63	0.65	0.0010	0.9980

The pseudo-homogeneous model showed a good fit for all three reaction systems where PTSA, rGO_H, and rGO_E were used as catalysts, as shown in Figure 6. Based on the values of the rate constants, forward (k_1) and reverse (k_2), as presented in Table 4, it is possible to suggest that this reaction tends to shift the equilibrium towards forming the reactants. The constant k_1 is related to the formation of solketal, and k_2 is associated with the reversibility of the reaction, with $k_2 > k_1$, meaning that the rate of product formation is slower than the rate that signifies the reversibility of the reaction towards the formation of the reactants. However, the difference in the equilibrium constant (K) values indicates that the reaction had not yet reached equilibrium, as evident when examining the calculated X_{Aeq} values from Equation (S9). The squared residuals (Q) below 0.01 indicate a low deviation between the experimentally obtained X_A data and the values of X_A calculated by the model; $X_{A\ EXP}$ and $X_{A\ CAL}$ are very close, validating the applied kinetic model. The determination coefficient values (R^2) being close to 1 indicate that the pseudo-homogeneous model can describe the experimentally obtained results, as shown in Figure 6.

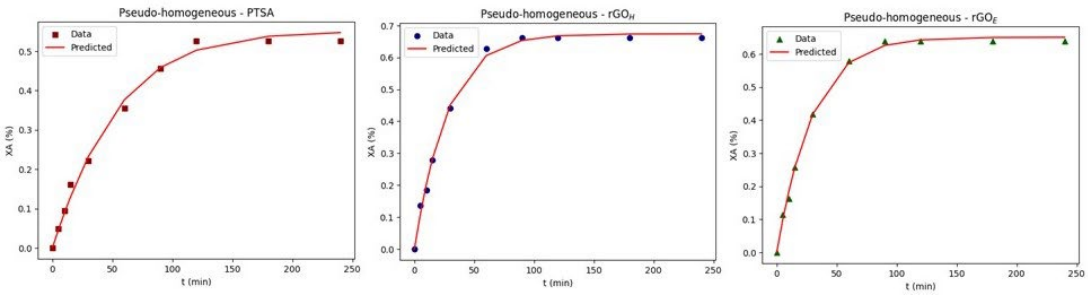

Figure 6. Pseudo-homogeneous models (data and predicted) applied to PTSA, rGO_H, and rGO_E were used as catalysts to produce the homogeneous catalyst (PTSA) and the heterogeneous catalysts (rGO_H and rGO_E). Conditions: glycerol/acetone molar ratio = 1:4; 5% catalyst relative to the mass of glycerol; 60 °C; 500 rpm with autogenous pressure; conducted in a 100 mL Parr reactor for 240 min.

The reversible model simplifies the complex kinetics of heterogeneous reactions by reducing the parameters so that k_1 and k_2 encompass all kinetic terms for the products and reactants, respectively. The pseudo-homogeneous model fits well with the heterogeneous rGO_H and rGO_E catalysts, but this does not imply that the catalysis is genuinely homogeneous. This happens because the surface of the heterogeneous catalyst is saturated with one of the reactants, in this case, acetone, as it is the excess reagent (glycerol/acetone molar ratio = 1:4). When there is an excess of reactant in the reactor, this excess can be much higher on the catalyst's surface. Thus, the model can be called pseudo-homogeneous. The literature has limited examples of modeling and kinetic studies using homogeneous or pseudo-homogeneous models for the glycerol ketalization reaction with acetone, and these are only for heterogeneous catalysts.

However, Esteban and coworkers [45] proposed a pseudo-homogeneous model and concluded that the reaction of $k_2 > k_1$ uses sulfonated resin as a catalyst. We observed the same conclusions regarding $k_2 > k_1$ in a study involving H-BEA zeolites in 2017, using a pseudo-homogeneous model programmed in Fortran, utilizing R2W [9].

The second approach used was heterogeneous kinetic modeling, aiming to gain insights into the rate-controlling step of the glycerol ketalization reaction with acetone (adsorption, chemical reaction, or desorption) when using heterogeneous catalysts of the rGO_H and rGO_E types. Once again, the reaction was considered to be of a bimolecular and reversible type. Dioxan was also disregarded in this study in an attempt to simplify the already complex heterogeneous model.

However, before proceeding with the modeling to estimate the kinetic parameters, some catalytic tests were conducted to determine whether the reaction was exclusively under kinetic control and free from external and internal diffusion limitations under the employed reaction conditions. The agitation (rpm) was varied, and glycerol conversion was monitored after 120 min of reaction, as shown in Figure 7.

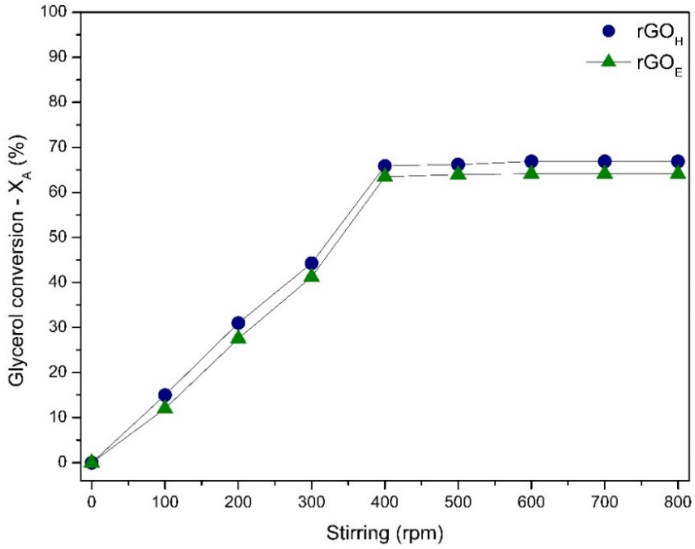

Figure 7. Results of glycerol conversion tests (XA%) as a function of agitation. (Glycerol/acetone molar ratio = 1:4; 5% catalyst based on glycerol mass; 60 °C; 100–800 rpm with autogenous pressure; conducted in a 100 mL Parr reactor for 120 min).

Figure 7 shows that between 400 and 800 rpm, glycerol conversion is free from external diffusion limitations. Additionally, internal diffusion limitations can also be disregarded within the agitation range of 500 rpm, as the kinetic diameters of the reactants and products of this reaction [9] are between 0.43 and 0.51 nm, and the average pore diameter of the catalysts used is around 10 nm, as indicated in Table 1.

The results of Figure 5 can be used to proceed with heterogeneous kinetic modeling using the rGO_H and rGO_E catalysts. In Nanda's studies (2014), for the same reaction, it was also observed that above 400 rpm, there was no influence of mass transfer [46]. The kinetic parameter results for each mechanism and the created models (Equations (S11)–(S23)) were estimated using Python programming language and the data from Figure 5.

Using Google Colab/Python language, it was possible to estimate the values for the rate constants, thermodynamic equilibrium constants, and the adsorption equilibrium constants of the reactants, as well as the desorption constants for the products, for two different catalytic systems (rGO_H and rGO_E). The estimated values are shown in Tables 5 and 6; LHHW and ER models, respectively.

Table 5. Results of the Estimated Kinetic Parameters for the glycerol ketalization reaction with acetone using the LHHW mechanism, considering the five proposed models (Equations (S13)–(S17)), using rGO_H and rGO_E catalysts. Conditions: 500 rpm; molar ratio 1:4 (G:A); 5% catalyst relative to the mass of glycerol; 240 min.

Catalyst	**Mechanism: LHHW**				
rGO_H	**Steep Control**				
Kinetic Parameters	**ADS, A**	**ADS, B**	**REACTION**	**DES, C**	**DES, D**
	Model 1	**Model 2**	**Model 3**	**Model 4**	**Model 5**
k (g_{cat} L mol^{-1} min^{-1})	0.0253	0.0027	0.5602	n	n
K	10.6544	0.1120	0.4063	n	n
K_A (L mol^{-1})	−3.3140	−0.5401	0.5473	n	n
K_B (L mol^{-1})	−0.0923	−0.2942	0.4391	n	n
K_C (L mol^{-1})	0.6902	0.5170	0.2468	n	n
K_D (L mol^{-1})	0.6912	0.5170	0.2468	n	n
Q	0.0007	0.0025	0.0017	-	-
R^2	0.9889	0.9940	0.9979	-	-

Table 5. *Cont.*

Catalyst	Mechanism: LHHW				
rGO_E	Steep Controlling				
Kinetic Parameters	ADS, A Model 1	ADS, B Model 2	REACTION Model 3	DES, C Model 4	DES, D Model 5
k (g_{cat} L mol^{-1} min^{-1})	0.0302	0.0028	0.5234	n	n
K	9.5613	0.1097	0.3512	n	n
K_A (L mol^{-1})	−1.7279	−0.4974	0.4851	n	n
K_B (L mol^{-1})	−0.0418	−0.2463	0.3522	n	n
K_C (L mol^{-1})	0.3599	0.3973	0.2150	n	n
K_D (L mol^{-1})	0.3602	0.3973	0.2150	n	n
Q	0.0007	0.0011	0.0008	-	-
R^2	0.9988	0.9975	0.9985	-	-

n = did not converge.

Table 6. Results of the Estimated Fitting Parameters for the glycerol ketalization reaction with acetone using the ER mechanism, considering the 6 proposed models (Equations (S18)–(S23)), using rGO_H and rGO_E catalysts. Conditions: 500 rpm; molar ratio 1:4 (G:A); 5% catalyst relative to the mass of glycerol; 240 min.

Catalyst	Mechanism: ER					
rGO_H	Steep Controlling					
Kinetic Parameters	ADS, A	ADS, B	SR, A	SR, B	DES, C	DES, D
	Model 6	Model 7	Model 8	Model 9	Model 10	Model 11
k (g_{cat} L mol^{-1} min^{-1})	0.0583	0.0089	0.0633	0.1693	n	n
K	10.6660	0.1100	0.4062	0.4063	n	n
K_A (L mol^{-1})	−7.2409	-	0.1535	-	n	n
K_B (L mol^{-1})	-	−0.1497	-	0.2658	n	n
K_C (L mol^{-1})	3.1890	-	0.0209	-	n	n
K_D (L mol^{-1})	-	0.1051	-	−0.0191	n	n
Q	0.0007	0.0031	0.0017	0.0017	-	-
R^2	0.9989	0.9944	0.9971	0.9971	-	-
Catalyst	Mechanism: ER					
rGO_E	Steep Controlling					
Kinetic Parameters	ADS, A Model 6	ADS, B Model 7	SR, A Model 8	SR, B Model 9	DES, C Model 10	DES, D Model 11
k (g_{cat} L mol^{-1} min^{-1})	0.0408	0.0093	0.0581	0.1531	n	n
K	9.5616	0.1092	0.3512	0.3512	n	n
K_A (L mol^{-1})	−2.3098	-	0.1479	-	n	n
K_B (L mol^{-1})	-	−0.3816	-	0.2745	n	n
K_C (L mol^{-1})	1.0152	-	0.0215	-	n	n
K_D (L mol^{-1})	-	1.5644	-	−0.0048	n	n
Q	0.0007	0.0012	0.0008	0.0008	-	-
R^2	0.9988	0.9975	0.9985	0.9985	-	-

n = did not converge.

The parameters' physical realism estimated through nonlinear regression was first considered to assess the proposed models' adequacy. This means that models that yielded negative values for any parameter and/or models that did not converge were discarded. To validate the model, the method chosen was the minimization of the sum of squared residuals (Q); see Equation (S10).

Upon observing Tables 5 and 6, it was found that the heterogeneous models created could only describe the kinetics of the heterogeneous reaction for the rGO_H and rGO_E

catalysts. Only one model was validated for each mechanism, as the other models resulted in one or more negative parameter values or did not converge and were thus discarded.

For the Langmuir-Hinshelwood-Hougen-Watson (LHHW) mechanism [47,48], the rate-controlling step of the reaction was the chemical reaction between the adsorbed reactants (A) glycerol and (B) acetone on the catalyst surface (R^2 = 0.9979; Q = 0.0017 for rGO_H and R^2 = 0.9985; Q = 0.0008 for rGO_E). This step can be considered a plausible rate-controlling step for the glycerol ketalization reaction with acetone.

As for the Eley-Rideal (ER) mechanism [45,49,50], the rate-controlling step of the reaction was the chemical reaction with only (B) acetone being adsorbed on the catalyst surface (R^2 = 0.9971; Q = 0.0017 for rGO_H and R^2 = 0.9985; Q = 0.0008 for rGO_E), which can also be considered a plausible rate-controlling step for the glycerol ketalization reaction with acetone. It is worth noting that the heterogeneous kinetic models were employed to predict which step serves as the rate-determining step for each of the mechanisms (LHHW and ER) used in the glycerol ketalization with an acetone reaction, not to estimate the value of each parameter involved physically.

It can be said that Model 3 (LHHW), Equation (S15), Model 8 (ER), and Equation (S20) all showed good fits for both the rGO_H and rGO_E catalysts. The squared residuals (Q) below 0.01 indicate a low deviation between the experimentally obtained X_A data and the X_A values calculated using the model. $X_{A\ EXP}$ and $X_{A\ CAL}$ are very close, validating the applied kinetic model. The values of the determination coefficients (R^2) very close to 1 indicate that the heterogeneous models can be employed to describe the experimentally obtained results, as shown in Figure 8.

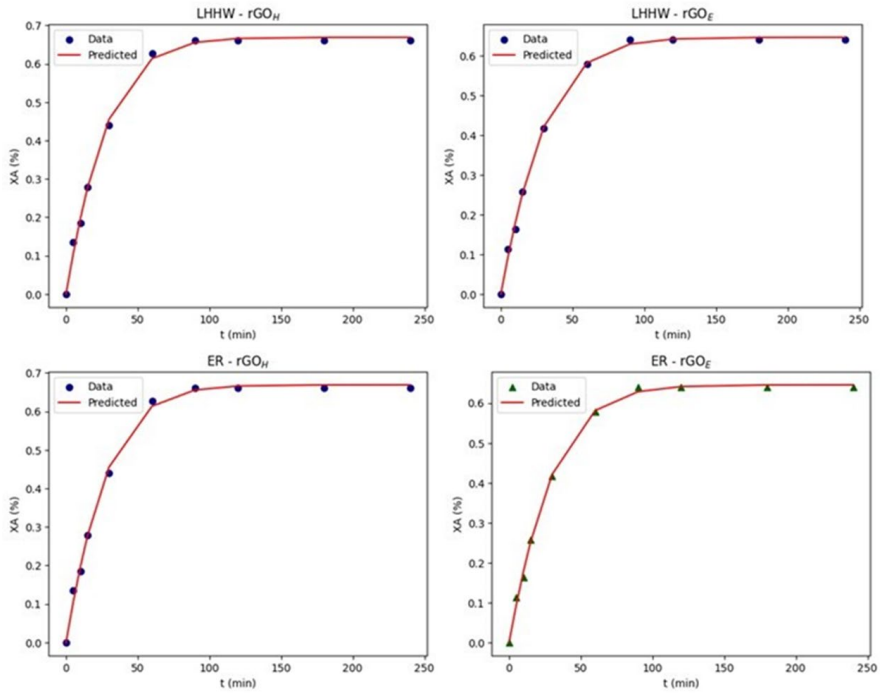

Figure 8. Kinetic heterogeneous models (data and predicted) applied to rGO_H and rGO_E were used as catalysts. Model 3 shows that the LHHW rate-controlling step of the reaction was the chemical reaction between the adsorbed reactants (A) glycerol and (B) acetone on the catalyst surface, and Model 8 shows that the ER rate-controlling step of the reaction was the chemical reaction with only (B) acetone being adsorbed on the catalyst surface. Conditions: glycerol/acetone molar ratio = 1:4; 5% catalyst relative to the mass of glycerol; 60 °C; 500 rpm with autogenous pressure; conducted in a 100 mL Parr reactor for 240 min.

The application of computational molecular modeling to study the mechanism of the glycerol ketalization reaction with acetone, using rGO_H and rGO_E as catalysts, would enable the confirmation of the mechanism and the rate-controlling step for this case. Studies

on the kinetics of the glycerol ketalization reaction with acetone using heterogeneous catalysts were conducted by the research group led by Nanda (2014) and by the group led by Esteban (2015) [45]. Nanda (2014) used Amberlyst 35 resin as the catalyst and employed the LHHW model to describe the glycerol ketalization reaction with acetone, with the chemical reaction as the rate-limiting step, which, with the adaptation of the data presented in this work, represents a plausible model [46]. On the other hand, the Esteban group (2015) concluded that the Eley–Rideal mechanism describes the glycerol ketalization reaction with acetone, with the chemical reaction involving the adsorption of only one of the reactants as the rate-limiting step of the reaction [45].

2.5. Study of Reuse of Heterogeneous Catalysts

Table 5 presents the results of the reuse tests for the rGO_H and rGO_E catalysts, and Table S4 displays the acidity results of the catalysts before and after the reuse tests. It is worth noting that the catalysts were initially separated from the reaction medium via filtration, without washing and drying, and were reused four times.

Table 5 presents the deactivation (reuse) study for the rGO_H and rGO_E catalysts, which exhibited the highest catalytic activities among the heterogeneous catalysts. There was a significant reduction in glycerol conversion, dropping from 66% to 23% for the rGO_H catalyst and from 64% to 30% for the rGO_E catalyst. This fact indicates that deactivation of the acidic sites of the material may have occurred, hindering the catalysis of the reaction. Additionally, the selectivity for solketal remained constant, averaging 80% for the rGO_E catalyst. However, the selectivity toward solketal for the rGO_H catalyst decreased from 98% to 91%, indicating an increase in dioxan selectivity.

Table S4 shows a significant decrease in the concentration of acidic sites in the rGO_H and rGO_E materials, which was directly proportional to their deactivations, as seen in Table 7. The highest deactivation for glycerol conversion was observed for the reduced graphene oxide prepared via Hummers method, i.e., a decrease from 66.18 to 23.18% after the fourth reuse (64.97% of total deactivation). The electrochemically exfoliated material presented a conversion decrease from 63.97% to 30.37% (a total deactivation of 52.68%). When the yields of solketal were considered, the former catalyst presented an overall deactivation of 67.47%, and the latter showed 54.12%, thus demonstrating the superiority of the rGO_E material as a catalyst for glycerol conversion. As possible causes of the deactivation, we can cite the water formation during the glycerol conversion and, consequently, the hydration of the acid sites (as observed via the reduction in the overall acidity, as seen in Table S4). We can also cite the possible sulfur leaching that the reaction reuses. However, despite this deactivation, we must highlight that both materials presented good conversions and yields even after the third reuse reaction.

Table 7. Results of reuse tests for the rGO_H and rGO_E catalysts for the glycerol conversion (X_A%), solketal selectivity (SS_5), and dioxan selectivity (SD_6), as well as the solketal yield (YS_5) and dioxan yield (YD_6).

Reactions	X_A (%)	SS_5(%)	SD_6 (%)	YS_5 (%)	YD_6 (%)
rGO_H	66.18 ± 0.45	98.38 ± 0.45	1.62 ± 0.45	65.11 ± 0.45	1.07 ± 0.45
rGO_H R_1	57.37 ± 0.85	95.60 ± 0.85	4.40 ± 0.85	54.85 ± 0.85	2.53 ± 0.85
rGO_H R_2	55.18 ± 0.45	94.38 ± 0.45	5.62 ± 0.45	52.08 ± 0.45	3.10 ± 0.45
rGO_H R_3	45.37 ± 0.85	94.62± 0.85	5.38 ± 0.85	42.93 ± 0.85	2.44 ± 0.85
rGO_H R_4	23.18 ± 0.45	91.38 ± 0.45	8.62 ± 0.45	21.18 ± 0.45	2.00 ± 0.45
Reactions	**X_A(%)**	**SS_5(%)**	**SD_6 (%)**	**YS_5 (%)**	**YD_6 (%)**
rGO_E	63.97 ± 0.86	80.73 ± 0.86	19.27 ± 0.86	51.64 ± 0.86	12.33 ± 0.86
rGO_E R_1	60.54 ± 0.43	80.64 ± 043	19.36 ± 0.43	48.82 ± 0.43	11.72 ± 0.43
rGO_E R_2	58.25 ± 0.32	81.03 ± 0.32	18.97 ± 0.32	47.20 ± 0.32	11.05 ± 0.32
rGO_E R_3	53.12 ± 0.28	79.27 ± 0.28	20.73 ± 0.28	42.11 ± 0.28	11.01 ± 0.28
rGO_E R_4	30.27 ± 0.13	78.25 ± 0.13	21.75 ± 0.13	23.69 ± 0.13	6.58 ± 0.13

(Glycerol/acetone molar ratio = 1:4; 5% catalyst based on glycerol mass; 60 °C; 500 rpm with autogenous pressure; 120 min; conducted in a 100 mL Parr reactor).

3. Materials and Methods

3.1. Materials

Glycerol (99.5% P.A.) and acetone (99.5% P.A.) were purchased from Proquímios (Rio de Janeiro, Brazil)®; solketal (98%) was purchased from Sigma-Aldrich® (St. Louis, MO, USA) and was used without further purification. Flake graphite, to produce rGO_H (synthesized via the Hummers method) [24,38,51], was purchased from Sigma-Aldrich and a carpentry pencil, to synthesize rGO_E (using the electrochemical process) [44,52], was acquired from the BIC® (São Paulo, Brazil).

3.2. Synthesis of Graphene-Derived Materials

3.2.1. Synthesis of Partially Reduced Graphene Oxide Using a Conventional Approach—rGO_H

Reduced graphene oxide (rGO_H) was synthesized using the modified Hummers method [24,38,51]. First, 100 mL of H_2SO_4 was added to a beaker with a volume of 1 L under an ice bath, and then 4 g of graphite flakes and 2 g of $NaNO_3$ were added and continually stirred at 450 rpm for 4 h. After this time, 12 g of $KMnO_4$ was slowly added, and the reaction mixture was kept for another 2 h, still under an ice bath. Then, the ice bath was removed, and the reaction system was heated at 35 °C for 30 min. Next, 160 mL of distilled and deionized water was dropped into the reaction mixture, and the reaction system was stirred for another 30 min. At this moment, the system's temperature increased to 90 °C. To finish the reaction, 160 mL of a 30% (*v/v*) H_2O_2 solution was added, and the suspension was then stirred for 12 h and subsequently washed and purified with distilled and deionized water, HCl (30% *v/v*), and ethanol until the supernatant pH reached 7.0. The suspension was filtered and the reduced graphene oxide was dried in an oven at 50 °C for 12 h. This material produced via a conventional approach was named rGO_H.

3.2.2. Synthesis of Partially Reduced Graphene Oxide via Electrochemical Method—rGO_E

The synthesis of the reduced graphene oxide was based on a study reported by Ambrosi and Pumera (2016) [20] in an acid medium. First, 1.0 mol L^{-1} of sulfuric acid was prepared. Afterward, a reaction system consisting of a 25 mL beaker and two graphite electrodes was set up. Some physical parameters were standardized, such as the distance between the graphite electrodes (3.5 cm), the height of each electrode at the bottom of the beaker (1 cm), the temperature (25 °C), the volume of sulfuric acid solution (20 mL), the voltage (10 V), and the time (1 h). After this time, the oxidized residue at the bottom of the beaker was removed from the reaction system, filtered, and washed until it reached the pH of distilled water, equal to 6.0, due to dissolved CO_2 [44,52]. Finally, the partially reduced graphene oxide was dried in an oven at 80 °C and named rGO_E.

3.3. Material Characterization

The materials rGO_H and rGO_E, along with their respective precursor graphites, were characterized using X-ray diffraction and a Bruker D2 Phaser (Rheinstetten, Germany) apparatus utilizing CuKα radiation (λ = 0.154 nm) with a Ni filter, scanning at intervals of 0.05° within the 2θ range of 5–50°. A convergent slit of 0.6 mm, a current of 10 mA, and a voltage of 30 kV were used with a Lynxeye detector (Oxford, Germany). Raman spectra were obtained using a Witec Alpha 300 R Raman Microscope (Oxford, Germany), with a wavelength of 532 nm (green light). Infrared spectra were collected using a Fourier-transform infrared spectrophotometer, Nicolet model Magna-IR 760 (Spectralab, Canada). Samples were analyzed via Attenuated Total Reflection (ATR) within the range of 400–4000 cm^{-1}, with 32 scans and a resolution of 4000 cm^{-1}.

Thermal analysis was conducted using a TA Instruments SDT Q 600 (Waters, Milford, MA, USA) instrument in the 25–800 °C temperature range, with a heating rate of 10 °C min^{-1} and an airflow of 50 mL min^{-1}. Textural analyses were performed on a Micromeritics Tristar 3000 Surface Area and Porosimetry Analyzer. (Micromeritics, Norcross, GA, USA) Samples were subjected to thermal drying at 90 °C under a vacuum of 5×10^{-3} torr for

24 h, and then cooled to room temperature and re-weighed to initiate analysis at −196 °C. Specific surface area was determined using the B.E.T. (Brunauer, Emmet, and Teller) method, while specific volume and pore diameter were found using the B.J.H. method from the adsorption/desorption isotherm [53].

Brønsted acidity was quantified through acid–base titration following the procedure described by Ventura and coworkers [40]. The surface acidity of the potential catalysts, rGO_H and rGO_E, was evaluated through acid–base titration. For the measurements, 50 mg of the material was weighed, and then 20 mL of a 0.05 mol L^{-1} sodium hydroxide solution was added. The mixture was stirred continuously for 24 h at room temperature. After this period, the solid was separated via centrifugation and the supernatant solution was titrated with hydrochloric acid (0.05 mol L^{-1}), using phenolphthalein as an indicator. The measurements were performed in triplicate. The precursor graphites were not analyzed in this step. The number of acidic sites on the catalyst was determined using Equation (1) [40]:

$$\text{Acidity} = [\text{Initial amount of NaOH added (mol)} - \text{Amount of HCl consumed (mol)}]/\text{mass of the material (g)}. \quad (1)$$

3.4. Catalytic Evaluation

The reactions were carried out in a Parr model 4848B stainless steel autoclave reactor (Parr Instrument Company, Moline, IL, USA) with a reaction volume of 100 mL. The reactor has a thermocouple, transducer, temperature controller, external heating mantle, and an agitation system; see Figure S1. Initially, a control test was conducted without a catalyst (blank). Subsequently, tests were performed using the homogeneous industrial catalyst p-Toluenesulfonic acid (PTSA) and the heterogeneous catalysts synthesized in this study, rGO_H, and rGO_E.

The reactor was loaded with 10 g of glycerol (0.1186 mol) and 25.2 g of acetone (0.4343 mol). Thus, the glycerol/acetone molar ratio (G:A) was 1:4. Catalyst loading of 5% by mass relative to the glycerol mass was used, corresponding to 500 mg. The agitation was set at 500 rpm, and the reaction was conducted at 60 °C with autogenous pressure for 120 min. The catalytic testing utilized a batch reactor with a thermocouple within the reaction vessel. This reactor, functioning as an autoclave-type system with precise temperature control, ensures the even dispersion of the catalyst within the fluid. The temperature measurement reflects the entire reaction system, which requires heating due to the endothermic nature of the reaction [46]. At the end of the reaction, 2.5 g of sodium bicarbonate was added to the reaction mixture to neutralize the catalyst (in the case of the homogeneous catalyst), and then the reaction mixture was filtered. Subsequently, the samples were stored at 15 °C for gas chromatography analysis. All reactions were performed in triplicate [9,54,55].

3.5. Study of Glycerol Conversion as a Function of Time

Since the reaction conditions had already been optimized in a study conducted by Rossa and coworkers [9,54,55] using other catalysts, the conversion study as a function of time was carried out under the same conditions as in Section 2.4. Samples were taken at intervals of 0, 5, 10, 15, 30, 60, 90, 120, 180, and 240 min. Subsequently, the samples were stored at 15 °C for gas chromatography analysis. All reactions were triplicated using PTSA, rGO_H, or rGO_E as catalysts.

3.6. Determination of Kinetic Parameter Models

3.6.1. Pseudo-Homogeneous Kinect Model

Tests for determining kinetic parameters in pseudo-homogeneous catalysis [9,56] were conducted using the rGO_H and rGO_E catalysts based on the time and glycerol conversion results in Section 3.5. (See "Pseudo-homogeneous Kinetic Model Evaluation" in Supplementary Materials.)

3.6.2. Heterogeneous Kinect Models (LHHW and ER)

In the heterogeneous model, initially, eight experiments were conducted under the same conditions as described in Section 3.4 for 60 min, only varying the agitation (100–800 rpm), and glycerol conversion was monitored to investigate the influence of external mass transfer and then predict how the internal mass transfer study was to be conducted. All reactions were performed in triplicate, and the samples were stored at 15 °C until the moment of analysis using GC-FID (Shimadzu, Japan).

The kinetic study of heterogeneous catalysis involves various physical steps (external and internal mass transfer) and chemical steps (adsorption, surface-catalyzed reaction, and desorption of products) according to the proposed mechanism. The study was conducted under reaction conditions free from diffusion limitations (external and internal mass transfer) in this stage. Tests for determining kinetic parameters in heterogeneous catalysis were performed using the rGO_H and rGO_E catalysts, based on the results obtained in Section 3.5, to predict the rate-limiting step of the reaction, both in the LHHW mechanism and in the ER mechanism.

We developed eleven heterogeneous kinetic models derived from two distinct Mechanism: LHHW (Langmuir-Hinshelwood-Hougen-Watson) and ER (Eley-Rideal) [57,58]. An adapted methodology from Shekara (2011) was employed [48]. (See "Heterogeneous Kinetic Model Evaluation" in Supplementary Materials.)

3.7. Study of Heterogeneous Catalyst Reuse

Deactivation/reuse tests [9,55] of the rGO_H and rGO_E catalysts were conducted under the same reaction conditions described in Section 2.4. The reuse tests involved using the same catalyst employed in 4 consecutive cycles without washing or calcination steps. All reactions were performed in triplicate, and the samples were stored at 15 °C until the analysis using GC-FID (Shimadzu, Japan) [9].

3.8. Product Analysis

The products of the glycerol ketalization reaction were quantitatively analyzed using a Shimadzu GC-FID equipped with a column Carbowax (30 m × 0.25 mm × 0.25 µm polyethylene glycol) and employing the external standard method [9,55]. Analysis conditions: total injection volume: 1 µL; injector: split/splitless; injection: automatic; linear velocity: 45 cm s^{-1}; split ratio: 1:50; linear velocity: 45 cm s^{-1}; sampling rate: 40 ms; carrier gas: helium; flow control mode: linear velocity; detector temperature: 250 °C; injector temperature: 250 °C. The heating ramp was set at 50 °C for 5 min, followed by a temperature increase from 50 °C to 180 °C at a rate of 16 °C per min. It was held at 180 °C for an additional 2 min, then increased from 180 °C to 230 °C at a rate of 20 °C per min, and then held at 230 °C for another 2 min. Total analysis time: 20 min.

The glycerol conversion and product selectivity were obtained using Equation (2).

$$X_A(\%) = \left(\frac{C_{A_0} - C_A}{C_{A_0}}\right) \times 100 \quad (2)$$

where C_{A0} is the initial molar concentration (mol L^{-1}) of glycerol and C_A is the final molar concentration (mol L^{-1}) of glycerol at the end of the reaction.

Solketal Selectivity (S_5, dioxolan):

$$Sel(S_5)\% = \left(\frac{AS_5}{AS_5 + AD_6}\right) \times 100 \quad (3)$$

where AS_5 is the area of solketal and AD_6 is the area of dioxan, obtained from the chromatograms. The areas of all of the compounds were previously adjusted using their respective correction factors.

Dioxan Selectivity (D_6):

$$\mathrm{Sel}(D_6)\% = \left(\frac{AD_6}{AS_5 + AD_6}\right) \times 100 \quad (4)$$

D_6 is the area of dioxan and AS_5 is the area of solketal, obtained from the chromatogram. The areas of all compounds were previously adjusted using their respective correction factors.

Yield—Y (%):

$$Y(\%) = (X_A \times S_i) \times 100 \quad (5)$$

S_i refers to the products S_5 or D_6, and X_A is the glycerol conversion (not in percentage) multiplied by the desired products' selectivity [9,55].

To calculate Turnover Frequency, Equation (6) was used.

$$\mathrm{TOF} = \frac{\frac{n_{A_0} - n_A}{n_{cat}}}{t} \quad (6)$$

where

n_{A_0} is the initial amount of glycerol (mol);
n_A is the amount of glycerol (mol) at the end of the reaction, after 2 h;
$n_{cat}$is the number of acid sites on the catalyst (mol $g_{cat}{}^{-1}$);
t is the time in hours (h);
TOF is the Turnover Frequency (h^{-1}).

4. Conclusions

This study effectively demonstrated the feasibility of replacing the homogeneous catalyst (PTSA) with the proposed heterogeneous catalysts (rGO_H and rGO_E). Remarkably, both rGO_H and rGO_E catalysts exhibited superior performance, achieving significant glycerol conversion and TOF values, outperforming PTSA. Additionally, the rGO_E catalyst demonstrated reusability over five consecutive cycles, showing the highest activity without the need for post-reaction washing or treatment. This suggests that an effective catalyst for the glycerol ketalization reaction with acetone should possess specific characteristics, including small crystal size, porosity, and acidity. The synthesis of rGO_E used a more environmentally friendly methodology, enabling its future utilization in various catalytic processes and providing the potential for chemical modifications, such as impregnation with transition metals and other compounds, to enhance its acidic properties.

The pseudo-homogeneous kinetic model successfully described the ketalization reaction of glycerol with acetone for both the homogeneous (PTSA) and heterogeneous (rGO_H and rGO_E) scenarios, with the model assuming a pseudo-homogeneous form for the heterogeneous catalysts. Among the eleven heterogeneous kinetic models explored to elucidate the mechanism and controlling step of heterogeneous kinetics, both of the rGO_H and rGO_E catalysts demonstrated positive results. Notably, Model 3 (LHHW) and Model 8 (ER) provided good fits for both of the rGO_H and rGO_E catalysts, offering valuable insights into the mechanism and controlling step of the heterogeneous catalytic reaction.

Supplementary Materials: The following supporting information can be downloaded at https://www.mdpi.com/article/10.3390/catal13111427/s1: Figure S1. Batch reactor used in all ketalization reactions (Parr Instruments Inc.—Model 4848B), made of stainless steel, with a useful volume of 100 mL, in a simple batch system, with a maximum working pressure of 200 bar. This reactor has a temperature and pressure controller. Also controlled agitation and external blanket for heating; Figure S2. Infrared spectra of graphite flakes (a) GRFH and reduced graphene oxide, (b) rGOH, obtained by the Hummers method; carpenter's pencil graphite (c) GFTE and reduced graphene oxide, (d) rGOE, obtained by the electrochemical method from carpenter's pencil graphite; Table S1. Estimated values for the distance between layers, average crystallite size, and number of layers for

GFTH, rGOH, GFTE and rGOE materials; Table S2. Assignments of the main bands in the infrared spectra for the GFTH, rGOH, GFTE and rGOE materials; Table S3. Acidity results obtained through acid-base titration for the materials tested as catalysts; Table S4. Acidity results for the catalysts obtained by acid-base titration before and after five reactions; Pseudo-Homogeneous Kinetic Model Evaluation; Heterogeneous Kinetic Model Evaluation; Langmuir-Hinshelwood-Hougen-Watson Mechanism (LHHW); Eley-Rideal Mechanism.

Author Contributions: Conceptualization, V.R., F.F.M. and V.G.d.C.M.; methodology, V.R., S.d.C.V., G.C.D., J.d.A.R., J.P.R.M., V.G.d.C.M. and F.F.M.; formal analysis, V.R., S.d.C.V., G.C.D., J.d.A.R., V.G.d.C.M. and F.F.M.; investigation, V.R., T.d.M.L., Y.R.C., J.L.N. and Y.X.; resources, T.d.M.L. and Y.R.C.; writing—original draft preparation, V.R. and J.d.A.R.; writing—review and editing, T.d.M.L., E.A.P. and V.R.; supervision, T.d.M.L.; project administration, T.d.M.L.; funding acquisition, T.d.M.L. All authors have read and agreed to the published version of the manuscript.

Funding: This study was financed in part by the Coordenação de Aperfeiçoamento de Pessoal de Nível Superior-Brasil (CAPES)—Finance Code 001—and CNPq and FAPERJ (E-26/211.575/2019; E26/203.188/2019, E-26/201.358/2021; E-26/210.315/2022).

Data Availability Statement: Data are contained within the article and Supplementary Materials.

Acknowledgments: The authors also acknowledge CNPq, FAPERJ, CAPES, Donato Aranda (EQ/UFRJ) and Sibele Pergher (IQ/UFRN).

Conflicts of Interest: The authors declare no conflict of interest.

References

1. Li, M.; Zheng, Y.; Chen, Y.; Zhu, X. Biodiesel Production from Waste Cooking Oil Using a Heterogeneous Catalyst from Pyrolyzed Rice Husk. *Bioresour. Technol.* **2014**, *154*, 345–348. [CrossRef] [PubMed]
2. Datta, I.; Ghosh, A.; Acharjee, A.; Rakshit, A.; Saha, B. Overview on Biodiesel Market. *Vietnam J. Chem.* **2021**, *59*, 271–284.
3. Galadima, A.; Muraza, O. A Review on Glycerol Valorization to Acrolein over Solid Acid Catalysts. *J. Taiwan Inst. Chem. Eng.* **2016**, *67*, 29–44. [CrossRef]
4. Muraza, O. Peculiarities of Glycerol Conversion to Chemicals Over Zeolite-Based Catalysts. *Front. Chem.* **2019**, *7*, 233. [CrossRef] [PubMed]
5. Corrêa, I.; Faria, R.P.V.; Rodrigues, A.E. Continuous Valorization of Glycerol into Solketal: Recent Advances on Catalysts, Processes, and Industrial Perspectives. *Sustain. Chem.* **2021**, *2*, 286–324. [CrossRef]
6. Zhang, H.; Hu, Z.; Huang, L.; Zhang, H.; Song, K.; Wang, L.; Shi, Z.; Ma, J.; Zhuang, Y.; Shen, W.; et al. Dehydration of Glycerol to Acrolein over Hierarchical ZSM-5 Zeolites: Effects of Mesoporosity and Acidity. *ACS Catal.* **2015**, *5*, 2548–2558. [CrossRef]
7. Fatimah, I.; Sahroni, I.; Fadillah, G.; Musawwa, M.M.; Mahlia, T.M.I.; Muraza, O. Glycerol to Solketal for Fuel Additive: Recent Progress in Heterogeneous Catalysts. *Energies* **2019**, *12*, 2872. [CrossRef]
8. Vojvodic, A.; Nørskov, J.K. New Design Paradigm for Heterogeneous Catalysts. *Natl. Sci. Rev.* **2015**, *2*, 140–143. [CrossRef]
9. Rossa, V.; Pessanha, Y.d.S.P.; Díaz, G.C.; Câmara, L.D.T.; Pergher, S.B.C.; Aranda, D.A.G. Reaction Kinetic Study of Solketal Production from Glycerol Ketalization with Acetone. *Ind. Eng. Chem. Res.* **2017**, *56*, 479–488. [CrossRef]
10. Kowalska-Kuś, J.; Held, A.; Nowińska, K. Solketal Formation in a Continuous Flow Process over Hierarchical Zeolites. *ChemCatChem* **2020**, *12*, 510–519. [CrossRef]
11. Alsawalha, M. Catalytic Activity and Kinetic Modeling of Various Modules HZMS-5 and Treated MCM-41 Catalysts, for the Liquid-Phase Ketalization of Glycerol with Acetone. *Front. Chem.* **2019**, *7*, 799. [CrossRef] [PubMed]
12. Rodrigues, R.; Santos, M.S.; Nunes, R.S.; Carvalho, W.A.; Labuto, G. Solvent-Free Solketal Production from Glycerol Promoted by Yeast Activated Carbons. *Fuel* **2021**, *299*, 120923. [CrossRef]
13. Chen, T.; Dai, L. Carbon Nanomaterials for High-Performance Supercapacitors. *Mater. Today* **2013**, *16*, 272–280. [CrossRef]
14. Yang, F.; Mao, J.; Li, S.; Yin, J.; Zhou, J.; Liu, W. Cobalt-Graphene Nanomaterial as an Efficient Catalyst for Selective Hydrogenation of 5-Hydroxymethylfurfural into 2,5-Dimethylfuran. *Catal. Sci. Technol.* **2019**, *9*, 1329–1333. [CrossRef]
15. Pei, S.; Wei, Q.; Huang, K.; Cheng, H.M.; Ren, W. Green Synthesis of Graphene Oxide by Seconds Timescale Water Electrolytic Oxidation. *Nat. Commun.* **2018**, *9*, 145. [CrossRef] [PubMed]
16. Achee, T.C.; Sun, W.; Hope, J.T.; Quitzau, S.G.; Sweeney, C.B.; Shah, S.A.; Habib, T.; Green, M.J. High-Yield Scalable Graphene Nanosheet Production from Compressed Graphite Using Electrochemical Exfoliation. *Sci. Rep.* **2018**, *8*, 14525. [CrossRef]
17. Marcano, D.C.; Kosynkin, D.V.; Berlin, J.M.; Sinitskii, A.; Sun, Z.; Slesarev, A.; Alemany, L.B.; Lu, W.; Tour, J.M. Improved Synthesis of Graphene Oxide. *ACS Nano* **2010**, *4*, 4806–4814. [CrossRef]
18. Song, J.; Wang, X.; Chang, C.-T. Preparation and Characterization of Graphene Oxide. *J. Nanomater.* **2014**, *2014*, 1–6. [CrossRef]
19. Kumar, S.; Wani, M.Y.; Koh, J.; Gil, J.M.; Sobral, A.J.F.N. Carbon Dioxide Adsorption and Cycloaddition Reaction of Epoxides Using Chitosan–Graphene Oxide Nanocomposite as a Catalyst. *J. Environ. Sci.* **2018**, *69*, 77–84. [CrossRef]

20. Maraschin, T.G.; Correa, R.d.S.; Rodrigues, L.F.; Balzarettid, N.M.; Malmonge, J.A.; Galland, G.B.; de Souza Basso, N.R.; Basso, N.R.d.S. Chitosan Nanocomposites with Graphene-Based Filler. *Mater. Res.* **2019**, *22*, 1–10. [CrossRef]
21. Schmal, M. *Heterogeneous Catalysis and Its Industrial Applications*, 1st ed.; Springer International Publishing: Cham, Switzerland, 2016; ISBN 978-3-319-09249-2.
22. Andonovic, B.; Temkov, M.; Ademi, A.; Petrovski, A.; Grozdanov, A.; Paunović, P.; Dimitrov, A. Laue Functions Model vs Scherrer Equation in Determination of Graphene Layers Number on the Ground of XRD Data. *J. Chem. Technol. Met.* **2014**, *6*, 545–550.
23. Andonovic, B.; Grozdanov, A.; Paunović, P.; Dimitrov, A.T. X-ray Diffraction Analysis on Layers in Graphene Samples Obtained by Electrolysis in Molten Salts: A New Perspective. *Micro Nano Lett.* **2015**, *10*, 683–685. [CrossRef]
24. Hummers, W.S.; Offeman, R.E. Preparation of Graphitic Oxide. *J. Am. Chem. Soc.* **1958**, *80*, 1339. [CrossRef]
25. Cobos, M.; González, B.; Fernández, M.D.J.; Fernández, M.D.J. Chitosan-Graphene Oxide Nanocomposites: Effect of Graphene Oxide Nanosheets and Glycerol Plasticizer on Thermal and Mechanical Properties. *J. Appl. Polym. Sci.* **2017**, *134*, 45092. [CrossRef]
26. Pattnaik, S.; Swain, K.; Lin, Z. Graphene and Graphene-Based Nanocomposites: Biomedical Applications and Biosafety. *J. Mater. Chem. B* **2016**, *4*, 7813–7831. [CrossRef]
27. Serhan, M.; Sprowls, M.; Jackemeyer, D.; Long, M.; Perez, I.D.; Maret, W.; Tao, N.; Forzani, E. Total Iron Measurement in Human Serum with a Smartphone. In Proceedings of the AIChE Annual Meeting, Orlando, FL, USA, 10–15 November 2019.
28. Kumar, A.S.K.; Jiang, S.-J. Chitosan-Functionalized Graphene Oxide: A Novel Adsorbent an Efficient Adsorption of Arsenic from Aqueous Solution. *J. Environ. Chem. Eng.* **2016**, *4*, 1698–1713. [CrossRef]
29. Sundramoorthy, A.K.; Vignesh Kumar, T.H.; Gunasekaran, S. *Graphene-Based Nanosensors and Smart Food Packaging Systems for Food Safety and Quality Monitoring*; In Graphene Bioelectronics; Elsevier: Amsterdam, The Netherlands, 2018; pp. 267–306.
30. Kumar, N.; Srivastava, V.C. Simple Synthesis of Large Graphene Oxide Sheets via Electrochemical Method Coupled with Oxidation Process. *ACS Omega* **2018**, *3*, 10233–10242. [CrossRef]
31. Malard, L.M.; Pimenta, M.A.; Dresselhaus, G.; Dresselhaus, M.S. Raman Spectroscopy in Graphene. *Phys. Rep.* **2009**, *473*, 51–87. [CrossRef]
32. Yang, X.; Tu, Y.; Li, L.; Shang, S.; Tao, X. Well-Dispersed Chitosan/Graphene Oxide Nanocomposites. *ACS Appl. Mater. Interfaces* **2010**, *2*, 1707–1713. [CrossRef]
33. Grande, C.D.; Mangadlao, J.; Fan, J.; De Leon, A.; Delgado-Ospina, J.; Rojas, J.G.; Rodrigues, D.F.; Advincula, R. Chitosan Cross-Linked Graphene Oxide Nanocomposite Films with Antimicrobial Activity for Application in Food Industry. *Macromol. Symp.* **2017**, *374*, 1600114. [CrossRef]
34. Zuo, P.-P.; Feng, H.-F.; Xu, Z.-Z.; Zhang, L.-F.; Zhang, Y.-L.; Xia, W.; Zhang, W.-Q. Fabrication of Biocompatible and Mechanically Reinforced Graphene Oxide-Chitosan Nanocomposite Films. *Chem. Cent. J.* **2013**, *7*, 39. [CrossRef] [PubMed]
35. Muda, M.S.; Kamari, A.; Bakar, S.A.; Yusoff, S.N.M.; Fatimah, I.; Phillip, E.; Din, S.M. Chitosan-Graphene Oxide Nanocomposites as Water-Solubilising Agents for Rotenone Pesticide. *J. Mol. Liq.* **2020**, *318*, 114066. [CrossRef]
36. Han, D.; Yan, L.; Chen, W.; Li, W. Preparation of Chitosan/Graphene Oxide Composite Film with Enhanced Mechanical Strength in the Wet State. *Carbohydr. Polym.* **2011**, *83*, 653–658. [CrossRef]
37. He, L.; Wang, H.; Xia, G.; Sun, J.; Song, R. Chitosan/Graphene Oxide Nanocomposite Films with Enhanced Interfacial Interaction and Their Electrochemical Applications. *Appl. Surf. Sci.* **2014**, *314*, 510–515. [CrossRef]
38. Sabzevari, M.; Cree, D.E.; Wilson, L.D. Graphene Oxide–Chitosan Composite Material for Treatment of a Model Dye Effluent. *ACS Omega* **2018**, *3*, 13045–13054. [CrossRef]
39. Tene, T.; Usca, G.T.; Guevara, M.; Molina, R.; Veltri, F.; Arias, M.; Caputi, L.S.; Gomez, C.V. Toward Large-Scale Production of Oxidized Graphene. *Nanomaterials* **2020**, *10*, 279. [CrossRef]
40. Ventura, W.M. Preparação de Catalizadores Heterogêneos a Base de Nb_2O_5 e CeO_2 Para Oxidação da Anilina Em Fase Líquida. Master's Thesis, Universidade Federal de Ouro Preto, Ouro Preto, Brazil, 2017.
41. Grassi, P.; Drumm, F.C.; Georgin, J.; Tonato, D.; Foletto, E.L. Preparação, Caracterização e Avaliação Catalítica Do Compósito Fe_2O_3/Grafite Em Reação Foto-Fenton Preparation (Characterization and Catalytic Evaluation of Fe_2O_3/Graphite Composite in Photo-Fenton Reaction). *Matéria* **2019**, *24*, e12434.
42. Fernando, P.; Braga, A.; Junqueira, A.; Dutra, B. Grafita. In *Rochas & Minerais Industriais - Usos e Especificações*; Luz, A.B.d., Lins, F.A.F., Eds.; CETEM-MCT: Rio de Janeiro, Brazil, 2008; pp. 527–549. ISBN 978-85-61121-37-2.
43. Ramesh, A.; Jeyavelan, M.; Leo Hudson, M.S. Electrochemical Properties of Reduced Graphene Oxide Derived through Camphor Assisted Combustion of Graphite Oxide. *Dalt. Trans.* **2018**, *47*, 5406–5414. [CrossRef]
44. Ambrosi, A.; Chua, C.K.; Latiff, N.M.; Loo, A.H.; Wong, C.H.A.; Eng, A.Y.S.; Bonanni, A.; Pumera, M. Graphene and Its Electrochemistry-an Update. *Chem. Soc. Rev.* **2016**, *45*, 2458–2493. [CrossRef]
45. Esteban, J.; Ladero, M.; García-Ochoa, F. Kinetic Modelling of the Solventless Synthesis of Solketal with a Sulphonic Ion Exchange Resin. *Chem. Eng. J.* **2015**, *269*, 194–202. [CrossRef]
46. Nanda, M.R.; Yuan, Z.; Qin, W.; Ghaziaskar, H.S.; Poirier, M.-A.; Xu, C.C. Thermodynamic and Kinetic Studies of a Catalytic Process to Convert Glycerol into Solketal as an Oxygenated Fuel Additive. *Fuel* **2014**, *117*, 470–477. [CrossRef]
47. Hougen, O.A.; Watson, K.M. *Chemical Process Principles Part There Kinetics and Catalysis*; John Wiley: New York, NY, USA, 1959.
48. Chandra Shekara, B.M.; Ravindra Reddy, C.; Madhuranthakam, C.R.; Jai Prakash, B.S.; Bhat, Y.S. Kinetics of Esterification of Phenylacetic Acid with p -Cresol over H-β Zeolite Catalyst under Microwave Irradiation. *Ind. Eng. Chem. Res.* **2011**, *50*, 3829–3835. [CrossRef]

49. Eley, D.D.; Rideal, E.K. Parahydrogen Conversion on Tungsten. *Nature* **1940**, *146*, 401–402. [CrossRef]
50. Miranda, C.; Urresta, J.; Cruchade, H.; Tran, A.; Benghalem, M.; Astafan, A.; Gaudin, P.; Daou, T.J.; Ramírez, A.; Pouilloux, Y.; et al. Exploring the Impact of Zeolite Porous Voids in Liquid Phase Reactions: The Case of Glycerol Etherification by Tert-Butyl Alcohol. *J. Catal.* **2018**, *365*, 249–260. [CrossRef]
51. Kauling, A.P.; Seefeldt, A.T.; Pisoni, D.P.; Pradeep, R.C.; Bentini, R.; Oliveira, R.V.B.B.; Novoselov, K.S.; Castro Neto, A.H. The Worldwide Graphene Flake Production. *Adv. Mater.* **2018**, *30*, 1–6. [CrossRef]
52. Ambrosi, A.; Pumera, M. Electrochemically Exfoliated Graphene and Graphene Oxide for Energy Storage and Electrochemistry Applications. *Chem. - A Eur. J.* **2016**, *22*, 153–159. [CrossRef]
53. Thommes, M.; Kaneko, K.; Neimark, A.V.; Olivier, J.P.; Rodriguez-Reinoso, F.; Rouquerol, J.; Sing, K.S.W. Physisorption of Gases, with Special Reference to the Evaluation of Surface Area and Pore Size Distribution (IUPAC Technical Report). *Pure Appl. Chem.* **2015**, *87*, 1051–1069. [CrossRef]
54. Rossa, V.; Treichel, H.; Alexandre, D.; Aranda, G. Transformation of Glycerol Into Solketal By Beta and Ferrierite Acid. *Perspect. EREXIM* **2017**, *41*, 101–112.
55. Rossa, V.; Díaz, G.C.; Muchave, G.J.; Aranda, D.A.G.; Berenice Castellã Pergher, S. Production of Solketal Using Acid Zeolites as Catalysts. In *Glycerine Production and Transformation—An Innovative Platform for Sustainable Biorefinery and Energy*; IntechOpen: London, UK, 2019; pp. 1–18.
56. Câmara, L.D.T.; Aranda, D.A.G. Reaction Kinetic Study of Biodiesel Production from Fatty Acids Esterification with Ethanol. *Ind. Eng. Chem. Res.* **2011**, *50*, 2544–2547. [CrossRef]
57. Fogler, H.S. *Elementos de Engenharia Das Reações Químicas*, 3rd ed.; Editora LTC: Rio de Janeiro, Brazil, 2002.
58. Hill, C.G., Jr. *An Introduction to Chemical Enginnering Kinetics & Reactor Design*; John Wiley & Sons: New York, NY, USA, 1997.